Article

Examining the Role of Atomic Scale Heterogeneity on the Thermal Conductivity of Transparent, Thermally Insulating, Mesoporous Silica–Titania Thin Films

Published as part of The Journal of Physical Chemistry virtual special issue "Emily A. Carter Festschrift".

Sophia C. King, Man Li, Tiphaine Galy, Yan Yan, Joon Sang Kang, Victoria M. Basile, Yolanda L. Li, Michal Marszewski, Laurent Pilon, Yongjie Hu, and Sarah H. Tolbert*

Read Online

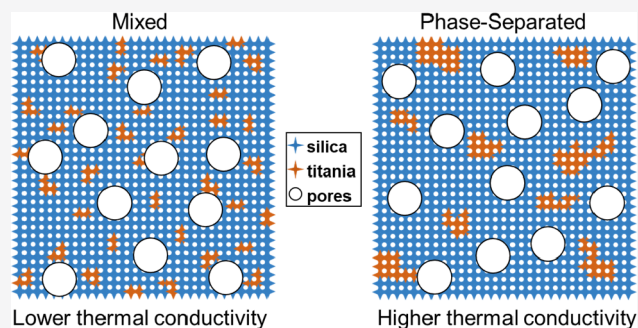ACCESS | Metrics & More | Article Recommendations | Supporting Information

ABSTRACT: This paper examines the effect of compositional heterogeneity on the thermal conductivity of transparent, mesoporous silica–titania composites that contain either 10 or 20 mol % titania. The relative hydrolysis rates of the silica and titania precursors were modified to control their compositional heterogeneity, while the ratio of polymer to inorganic precursors (silica + titania) was varied to control the porosity of the films. All films were optically transparent at thicknesses up to 1 μm with transmittance above 90% and haze below 5% at visible wavelengths. It was found that the heterogeneity of the titania species in the 10 mol % titania samples could be easily tailored from highly dispersed titania to a composition with heterogeneous silica-rich and titania-rich domains.

By contrast, samples with 20 mol % titania always showed a heterogeneous titania distribution. The results show that mesoporous films with more homogeneously distributed titania had a lower thermal conductivity at all porosities, likely due to increases in propagon and diffuson scattering as a result of the increased number density of titania heteroatom scattering centers. These results increase our understanding of heat carrier propagation in amorphous materials and add to the design rules for creating amorphous, optically clear, low thermal conductivity materials.

INTRODUCTION

Using materials as thermal insulation to separate hot from cold is a pursuit as old as humankind. As rocks, wood, and fur have given way to designer materials, so have the challenges that can be addressed. This includes creating materials with extraordinarily low thermal conductivity[1−3] and creating materials that can survive at extremely high temperatures.[4−7] In this work, we tackle another challenge in this field, which is the optimization of materials with both low thermal conductivity and high optical clarity for applications such as window insulation. Here we specifically focus on templated nanoporous networks made from combinations of amorphous silica and titania and explore the role of compositional heterogeneity in controlling thermal conductivity.

Crystalline materials are often good conductors of heat because their long-range atomic-scale order facilitates heat carrier propagation via lattice vibrations (or phonons).[8−10] In amorphous materials, however, the disorder and randomized atomic positions are not conducive to phonon transport, resulting in a significantly reduced mean free path for the carriers. In such systems, heat is transferred via propagons (propagating vibrational modes that are similar to phonons but with much shorter mean free paths), diffusons (delocalized, but nonpropagating vibrational modes), and, to a lesser extent, locons (localized vibrational modes).[8−12] To further reduce the thermal conductivity of amorphous materials, one must decrease heat carrier mobility. Often, this is achieved by making a material porous, which reduces the effective density of the material and, as a result, heat carrier transport.[12,13] Porosity also has the added benefits of increasing internal surfaces, which can act as scattering centers, and of spatial confinement of heat carriers, both of which can be reasonably well accounted for in crystalline materials with well-defined phonon distributions.[14,15] By contrast, the fundamental relationship between the structure of amorphous, porous
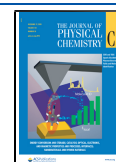
materials and their thermal conductivity is still not well understood beyond the aforementioned density effects.[12,16]

As a result, improving thermal resistance in porous insulators is typically achieved by increasing their porosity, which often negatively impacts other performance metrics and limits practical application of the resulting materials. For instance, silica aerogels can reach thermal conductivities as low as 0.015 W m^{-1} K^{-1} under ambient conditions when the porosity exceeds 95%.[17] However, such large porosity results in poor mechanical integrity of aerogels.[1,18,19] In addition, the large pores that form in connection with the increased porosity strongly scatter visible light, rendering aerogels opaque or translucent.[19,20] Thus, establishing new methods for reducing thermal conductivity of porous insulators is of paramount importance and can lead to the development of better thermal insulators with both mechanical robustness and high optical transparency for applications in energy-saving architectural glass[21] and solar–thermal energy conversion systems.[22]

Many structural effects on thermal conductivity in templated mesoporous materials have already been reported, such as the role of precursor type (discrete nanocrystals vs continuous sol–gel), wall thickness, and pore packing (cubic vs hexagonal).[23–26] In nontemplated porous silica, the fractal dimension has also been shown to influence the thermal conductivity.[27–29]

In bulk systems, composition can also be used to reduce thermal conductivity. For example, in crystalline materials, the addition of point defects in the form of atomic or isotopic dopants has been computationally and experimentally shown to scatter phonons at the boundaries of the defects.[5,30–34] Seyf and Henry computationally showed that as the concentration of defects increases in a crystal, the population of propagating modes rapidly changes to nonpropagating diffusons and locons.[34] This decrease in phonon propagation leads to a reduction in the thermal conductivity of the material. For amorphous systems, Choy et al. measured the thermal conductivity of different metallic glasses and separated the electronic and nonelectronic contributions to the thermal conductivity.[35,36] They found that for metal–metalloid glasses, the thermal conductivity decreased as more chemical elements were added to the alloy. More specifically, they found that the nonelectronic or vibrational component of the thermal conductivity decreased significantly as the complexity of the chemical composition increased. This was attributed to increased vibrational scattering with increases in the degree of disorder due to the large number of components of the alloys. While these studies demonstrate that the thermal conductivity of crystals and amorphous insulators can be reduced using compositional heterogeneity, the thermal conductivities reported were all greater than 5 W m^{-1} K^{-1} because the materials studied were either crystalline or metallic. As a result, it is still not clear if compositional heterogeneity in a material can have a significant impact in ultralow thermal conductivity applications.

Unfortunately, it is quite challenging to find systems suitable for the study of solid-solution effects on thermal conductivity in materials with thermal conductivities on the order of 0.1 W m^{-1} K^{-1}. To begin with, there is a small range of amorphous oxides that mix well enough to form solid solutions with variable heterogeneity.[37,38] Ideally, we would like to use a silica-based network because, in addition to being transparent, they are intrinsically amorphous and easy to form into nanoporous networks with controllable pore sizes—all

favorable properties for low thermal conductivity. We then need to add another metal oxide that can form a well-mixed network, while maintaining the favorable low thermal conductivity and optical properties. Mesoporous silica–titania composites have been studied as thermal insulators,[3,39] and the synthesis of silica–titania glasses has been rigorously explored for optical, electronic, and catalytic applications.[40–44] It has been shown by using X-ray absorption near edge structures (XANES), extended X-ray absorption fine structures (EXAFS), Fourier transform infrared spectroscopy (FTIR), nuclear magnetic resonance spectroscopy (NMR), and X-ray photoelectron spectroscopy (XPS) that at low concentrations of titania (<15 mol %), silica–titania forms a solid solution when synthesized by sol–gel based methods.[45–51] Moreover, the heterogeneity of the silica–titania network can be controlled at these low concentrations of titania (<15 mol %) by tailoring the relative hydrolysis rates of the molecular precursors for silica and titania.[46,50,51] Finally, when annealed at moderate temperatures (<450 °C), the crystallization of titania can be suppressed at large silica concentrations.[42,43,52] Silica–titania is therefore the ideal system for this study as it allows us to create amorphous, porous materials with variable homogeneity and good optical quality.

With these ideas as a backdrop, this study aims to elucidate the effect of chemical homogeneity on the thermal conductivity of mesoporous silica–titania composites. To do so, mesoporous silica–titania thin films were synthesized with either 10 or 20 mol % titania, at porosities ranging from to 25 to 60%. For the samples made with 10 mol % titania, the level of homogeneity was controlled by varying the relative hydrolysis rates of the silica and titania precursors. Given the limited solubility of titania in silica at concentrations exceeding 15 mol %, the samples made with 20 mol % titania acted as a control to assess the effect of the synthetic methods on thermal conductivity, as these samples should show phase-separated titania across all synthetic conditions. The structure of the films was characterized with scanning electron microscopy (SEM), transmission electron microscopy (TEM), ellipsometric porosimetry, optical interfereometry, optical interfereometry, and two-dimensional grazing incidence small-angle X-ray scattering (2D-GISAXS). Their composition and homogeneity were characterized with energy-dispersive X-ray spectroscopy (EDS), XPS, solid state ^{29}Si NMR, and FTIR. Finally, their effective thermal conductivity was measured using time-domain thermoreflectance (TDTR).

■ METHODS

Materials. The following materials were obtained from commercial suppliers and used without further purification: triblock copolymer Pluronic F127 (PEO$_{100}$PPO$_{65}$PEO$_{100}$, M_w = 12600, BASF), tetraethyl orthosilicate (TEOS, 98%, Acros Organics), titanium isopropoxide (TIPO, 98%, Acros Organics), 2,4-pentanedione (acetylacetone, 99%, Acros Organics), 2,4-pentanedione (acetylacetone, 99%, Acros Organics), hydrochloric acid (Certified ACS Plus, Fisher Scientific), and ethanol (EtOH, 200 proof, Rossville Gold Shield).

Synthesis. The synthesis of mesoporous silica–titania mixed films was adapted from the works of Dong et al. and Dunphy et al.[43,53] F127:EtOH:HCl:H$_2$O:TIPO:TEOS were combined in a 7.4:50:6.1:0.06:x:(1 − x) molar ratio, where x is 0.1 or 0.2. In a typical synthesis of silica–titania with molar ratio 90−10 and m_{poly}/m_{inorg} = 1.5 g/g, 280 mg of Pluronic surfactant F127 (PEO$_{100}$PPO$_{65}$PEO$_{100}$) was first added to 6

mL of ethanol, 0.325 mL of doubly distilled water, and 0.425 mL of 37% HCl under rapid stirring at 60 °C until the polymer was fully dissolved. Then, 0.62 mL of TEOS was added to the reaction mixture, followed by the dropwise addition of 0.1 mL of TIPO. The reaction was left to stir for 5 h at 60 °C.

To increase the compositional homogeneity of the mixture, a modified synthesis was adapted from Chen et al.[51] In the modified synthesis of silica−titania with molar ratio 90−10 and m_{poly}/m_{inorg} = 1.5 g/g, 0.1 mL of TIPO was combinreaction mixture, followed by the dropwise additioned with 0.03 mL of acetylacetone in 1 mL of ethanol and stirred for an hour at 60 °C. Concurrently, in a separate flask, 0.62 mL of TEOS was combined with 0.053 mL of H_2O in 1 mL of ethanol and stirred for an hour at 60 °C. Then, both solutions were added to a solution of 280 mg of F127 in a mixture of 4 mL of ethanol, 0.27 mL of water, and 0.425 mL of 37% HCl and stirred for 4 h. Full details of the regular and modified syntheses are included in Table S1.

To obtain films of thicknesses >200 nm, the solutions were concentrated by rotary evaporation at 80 mTorr in a 60 °C temperature bath for 10 min. Films were made by spin coating the solutions onto silicon wafers or 1 mm thick glass microscope slides. The films were then calcined under flowing O_2 by first holding at 350 °C for 6 h and then at 400 °C for 2 h to remove all polymer template and ensure that the titania was in its fully oxidized form. A ramp rate of 2 °C min^{-1} was used for both heating and cooling.

Substrate free powdered samples for NMR and FTIR analyses were made by evaporating the same solutions used for film formation in Petri dishes for 3−7 days at humidity >50%. The resulting powders were then calcined in flowing O_2 at 400 °C for ∼12 h (until all of the polymer was removed).

Characterization. The structure of the samples was examined with scanning electron microscopy (SEM), transmission electron microscopy (TEM), ellipsometric porosimetry, N_2 porosimetry, two-dimensional grazing incidence small-angle X-ray scattering (2D-GISAXS), and two-dimensional grazing incidence wide-angle X-ray scattering (2D-GIWAXS). The composition and chemical bonding were further examined using EDS, XPS, solid-state ^{29}Si NMR, and FTIR. The thermal conductivity was measured using a time domain thermoreflectance (TDTR) technique, with the specific heat capacity c_p of representative powdered measured through differential scanning calorimetry (DSC). The full details of these characterization methods are given in the Supporting Information.

RESULTS AND DISCUSSION

Using polymer templating methods at acidic pH, sol−gel based mesoporous silica−titania (ST) films were synthesized at ratios of 10 mol % (ST10) and 20 mol % titania (ST20). The hydrolysis rate of the silica precursor, tetraethyl orthosilicate (TEOS), is much slower than that of the titania precursor, titanium isopropoxide (TIPO), leading to the formation of titania-rich nanodomains in the solid network when these precursors are simply mixed. The homogeneity of the titania within the matrix can, however, be adjusted by tuning the hydrolysis rates of their molecular precursors.[43] Specifically, at concentrations less than 15 mol % of titania, a more homogeneous network of silica−titania can be obtained by simultaneously increasing the hydrolysis rate of TEOS through prehydrolysis with water, while reducing the hydrolysis rate of TIPO through the use of a chelating ligand such as

acetylacetone.[38,46,49,51] This method was applied to mesoporous silica−titania films with ratios of 10 and 20 mol % titania. The full synthetic details are given in Table S1 of the Supporting Information, where the samples were labeled as regularly synthesized (reg), where the silica and titania precursors were just mixed and added to the network, or modified (mod) where the synthesis was modified such that the hydrolysis rates of the precursors were better matched. The 20 mol % titania samples served as a control for the differences in synthetic method, as this sample should have titania-rich nanodomains with both synthetic methods because of the high titania concentration.

Structural Characterization. The SEM images of the ST10reg and ST20reg composites in Figures 1a and 1b show
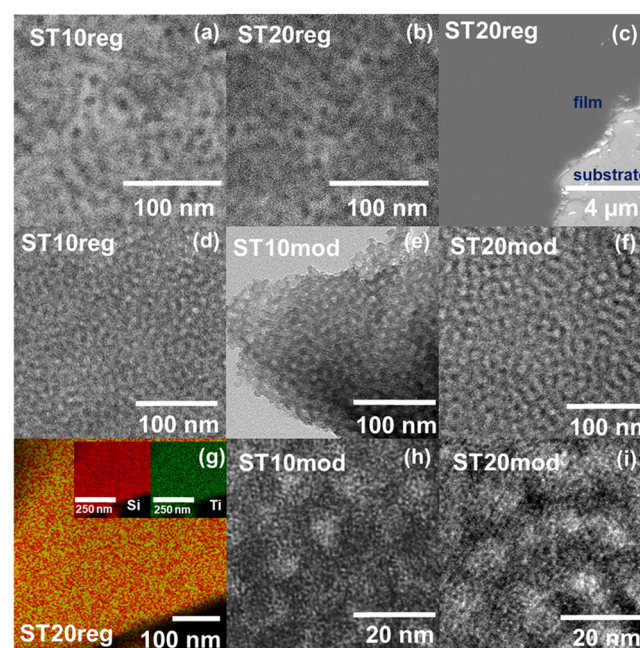

Figure 1. Electron micrographs and electron spectroscopy showing the structure and composition of the mesoporous silica−titania composites. (a, b) Scanning electron micrograph (SEM) of (a) an ST10reg and (b) an ST20reg sample showing the porous structure. (c) Low-magnification SEM image of a typical ST20reg sample showing the homogeneity and lack of large scale defects in these porous films. (d−f) Transmission electron micrographs (TEM) of a typical (d) ST10reg, (e) ST10mod, and (f) ST20mod sample also showing the porous structure. (g) Energy-dispersive X-ray spectroscopy (EDS) map of an ST20reg sample showing good mixing in the silica−titania composite. (h, i) High-resolution TEM (HR-TEM) of a typical (h) ST10reg and (i) ST20mod sample showing a lack of lattice fringes in the amorphous pore walls of these samples.

that homogeneous mesoporous silica−titania composite films were successfully synthesized. As shown in the low-magnification image in Figure 1c, the synthesized films are smooth and lack significant defects such as cracks, phase separation, or large pores, which is favorable, as these features would scatter light.[54] The TEM images in Figures 1d−f indicate that all porous silica−titania network was continuous, with homogeneously dispersed small pores; this is true for both the regular and modified syntheses. The EDS map of a typical ST20reg film in Figure 1g shows that the silica−titania composite was well mixed at the resolution of EDS mapping (∼20 nm), even for the ST20 films, which we expect to show

the most phase separation. Data for ST10reg are similar (see Figure S1). This indicates that other methods will need to be employed to quantify compositional heterogeneity in these films. The lack of lattice fringes in the HR-TEM images of Figures 1h and 1i further suggests that the titania remained amorphous in both the ST10reg and ST20reg samples. This is corroborated by the lack of diffraction peaks in the reduced two-dimensional grazing incidence X-ray scattering (2D-GIWAXS) data in Figure S2. This lack of crystallinity of titania was expected since the presence of a high percentage of silica has been shown to suppress the crystallization of titania.[43] Additionally, the films were calcined at 400 °C, a relatively low temperature for titania crystallization.[52,55−58]

We conducted transmittance and haze measurements to further examine the optical quality of films coated on 1 mm thick glass microscope slides. Here the total transmittance of the films quantifies the percent of light transmitted through the film, including light lost to reflection, while haze is a measure of the clarity of the material and quantifies only scattering (see the Supporting Information for more details). In general, films of good optical quality have transmittance above 90% and haze below 5%.[54] Figure 2 compares the normal-hemispherical
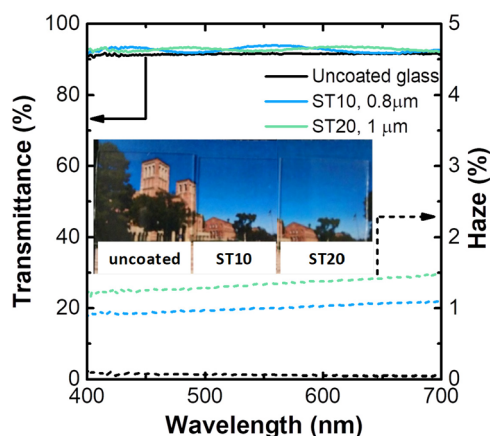

Figure 2. Normal-hemispherical transmittance−haze measurements across the visible spectrum for uncoated glass and typical ST10 and ST20 samples. Photos of the uncoated glass and ST10 and ST20 samples are shown in the inset.

transmittance and haze of typical ST10 and ST20 films to that of an uncoated glass slide along with photographs of the films. Both coated samples featured similar high transmittance values in excess of 90%. The ST10-coated sample had a haze on the order of 1%, which is lower than the ST20-coated sample. Because both coated samples had haze values that were below 2%, they do not significantly scatter light in the visible regime and are therefore suitable as coatings for applications where optical transparency is desired.

To quantify the degree of heterogeneity in the silica−titania films, solid-state ^{29}Si NMR and FTIR were used to examine local bonding between Si and Ti; this was done because EDS mapping was unable to resolve the heterogeneity in the composites. In a typical ^{29}Si NMR spectrum, the Q peaks are indicative of Si−O−M bonds, where M represents any atom. A Q^4 peak indicates a Si atom bonded to only O−Si moieties. A Q^3 peak indicates a Si atom with three such bonds and one O−heteroatom bond, such as the Ti in our system. The ratio of the areas of the Q^3/Q^4 peaks can be used to quantify homogeneity. Given the same silica−titania ratio, a higher ratio

of Q^3/Q^4 peaks indicates that titania is more homogeneously distributed in the silica network at the atomic scale. By contrast, when silica and titania separate into two phases, they form more Si−O−Si and Ti−O−Ti and less Si−O−Ti bonds. FTIR can also be used to study the homogeneity of the mixed system by directly probing the absorption of the Si−O−Ti stretch. The greater the intensity of the stretch, the greater the number of Si−O−Ti bonds and the more homogeneously distributed the titania. As such, both methods can be used to quantitatively determine the extent to which titania is distributed in the silicate structure.

The NMR spectra plotted in Figures 3a and 3b indicate that the relative Q^3/Q^4 peak area ratio for the ST10mod sample was 0.71 (Figure 3b), while it was only 0.60 for the ST10reg sample (Figure 3a). This suggests that there is a more homogeneous distribution of titania in the solid network produced when the hydrolysis rates of the molecular precursors were better matched. Likewise, the stronger intensity of the Si−O−Ti stretching absorption band at 950 cm^{-1} for the ST10mod film compared to the ST10reg film (Figure 3c) confirms that titania in the modified sample is indeed more homogeneously distributed. By contrast, modifying the synthesis of the ST20 films had no significant effect on the distribution of titania in the silica matrix. While the Q^3/Q^4 area ratios are higher for all the ST20 samples due to the larger titania content, both ST20reg and ST20mod films had comparable Q^3/Q^4 area ratios of 0.78 and 0.79, respectively, according to the NMR spectra plotted in Figures 3d and 3e. Similarly, the intensities of the Si−O−Ti IR absorption bands were the same for the ST20reg and ST20mod samples plotted in Figure 3f. The similarity of ST20reg and ST20mod was likely due to the limited solubility of titania in silica at 20 mol % which has been reported in the literature.[49] As a result, unlike the ST10 films, the homogeneity of the ST20 films could not be tailored by controlling the hydrolysis rates of the molecular precursors. The ST20 samples are thus ideal experimental controls to determine whether changes in thermal conductivity, discussed below, should be attributed primarily to changes in the titania distribution within the material or are simply due to differences in the synthetic method. Overall, using a templated sol−gel based method yielded amorphous, mesoporous silica−titania films with good optical quality and controllable atomic-scale mixing of the silica and titania in the network at low titania concentrations.

X-ray photoelectron spectroscopy was conducted to further quantify the ratio of silica:titania, as well as to quantify any defects in the mixed, mesoporous structure. High-resolution XPS spectra of the Si 2p peak, the Ti 2p peaks, and O 1s peak from representative ST10reg, ST10mod, ST20reg, and ST20mod samples are depicted in Figure S3. A summary of the deconvoluted peak positions and their respective areas and relevant ratios are given in Table 1. The area ratios of the Si 2p and Ti 2p peaks were used to quantify the ratio of Si:Ti on the surface of the films. The ratios of Si:Ti were found to be 90:10, 89:11, 85:15, and 83:17 on the surface of the ST10reg, ST10mod, ST20reg, and ST20mod films, respectively. For the ST10 samples, these compositions are in good agreement with those determined from EDS (92:8 ± 2), confirming that there is little to no enrichment of Si or Ti on the surface of the films compared to the bulk material. For the ST20 samples, however, the Ti content (15% for ST20reg, 17% for ST20mod) is lower than determined from EDS (80:20 ± 1), likely as a result of surface enrichment with Si. We hypothesize
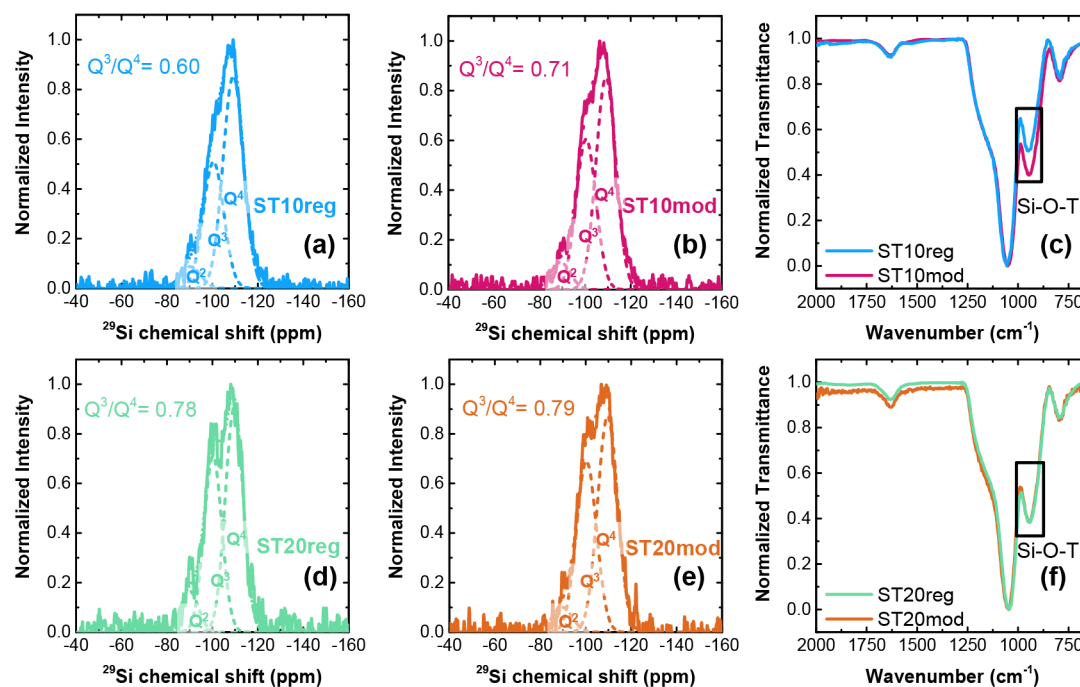
Figure 3. Examining the effect of synthesis parameters on the homogeneity of mesoporous mixed silica−titania powders. (a, b) Solid-state ^{29}Si NMR with the Q^3/Q^4 peak area ratio shown as an inset for ST10 powders made by using the regular and modified synthetic methods, respectively. (c) FTIR absorption for ST10reg and ST10mod showing differences in the Si−O−Ti vibrational mode. (d, e) Solid-state ^{29}Si NMR with the Q^3/Q^4 peak area ratio again shown as an inset for ST20 powders made by using the regular and modified synthetic methods, respectively. (f) FTIR absorption for ST20reg and ST20mod showing no differences in the intensity of the Si−O−Ti vibrational mode.

Table 1. Peak Positions and Areas Obtained from XPS for the Four Mesoporous Silica−Titania Composites Explored in This Work

peak designation	sample	ST10reg	ST10mod	ST20reg	ST20mod
Si 2p	peak position (eV)	103.5	103.7	103.3	103.1
	peak area	23.78	23.88	21.76	21.40
Ti 2p$_{1/2}$$^{3+}$	peak position (eV)	464.0	463.7	463.1	463.4
	peak area	0.10	0.09	0.03	0.09
Ti 2p$_{1/2}$$^{4+}$	peak position (eV)	465.5	465.5	465.1	465.0
	peak area	0.79	0.85	1.22	1.36
Ti 2p$_{3/2}$$^{3+}$	peak position (eV)	458.3	457.9	457.3	457.4
	peak area	0.20	0.18	0.06	0.19
Ti 2p$_{3/2}$$^{4+}$	peak position (eV)	459.8	459.7	459.3	459.2
	peak area	1.58	1.70	2.43	2.73
O 1s Ti−O	peak position (eV)	530.9	531.0	530.8	530.6
	peak area	5.19	5.14	9.99	11.01
O 1s Si−O	peak position (eV)	532.6	532.7	532.6	532.4
	peak area	68.36	68.15	64.52	63.22
relative area ratio Si 2p:Ti 2p (%)		90:10	89:11	85:15	83:17
relative area ratio Ti 2p^{4+}:Ti 2p^{3+} (%)		89:11	90:10	98:02	94:06
relative area ratio Si−O:Ti−O (%)		93:07	93:07	87:13	87:13
O 1s/(Si 2p + Ti 2p)		2.78	2.74	2.92	2.88

that since the titania precursors hydrolyze faster than those of silica, they may form small titania domains, which then get encapsulated by the silica when it eventually hydrolyzes and condenses, leading to surface Si enrichment.

Additional insight could be gained by examining the peak shift and other relative area ratios in each spectrum. The Si 2p peak positions (Figures S3a,d,g,j) are all lower than that of pure silica (104.1 eV).[45] These shifts to lower binding energies are expected, since Ti is less electronegative than Si (1.5 for Ti vs 1.9 for Si). When we compare the ST10 films with peaks centered at 103.5−103.7 eV to those from ST20 samples that have peak positions at 103.1−103.4 eV, we observe a slightly larger shift for the ST20 samples, consistent with the higher Ti content.

Next, we look at the Ti 2p peaks to elucidate the fraction of nonoctahedral titania in the network. The typical Ti 2p peaks are split into Ti 2p$_{1/2}$ and Ti 2p$_{3/2}$ as a result of spin−orbit coupling, as shown in Figures S3b,e,h,k. Deconvolution of these peaks shows that while the films are made up primarily of Ti^{4+}, there is some Ti^{3+} present from TiO$_x$ species where $x < 2$. These TiO$_x$ species arise from defects in the structure as a result of the incorporation of octahedral titania into tetrahedral silica sites.[59] To quantify the nonoctahedral titania, we calculated the ratio of Ti 2p^{4+}:Ti 2p^{3+}. The ST10reg, ST10mod, ST20reg, and ST20mod samples have Ti 2p^{4+}:Ti 2p^{3+} ratios of 89:11, 90:10, 98:2, and 96:4, respectively. The data indicate that there is significantly more Ti^{3+}, suggesting more nonoctahedral titania, in the ST10 samples than the ST20 materials. This observation was expected, as the ST10 samples were better mixed and contained smaller titania domains than the ST20 films. We believe that the smaller domains of the ST10 films consisted of more frustrated titania species in the silica network, while the larger titania domains in

the ST20 films would contain a greater number of stable Ti–O–Ti bonds and overall more octahedral titania in the network. The similarity of the ST10reg and ST10mod samples, however, indicates that nonoctahedral titania is not primarily responsible for the differences in thermal conductivity presented below.

Finally, we examine both the relative ratios and peak shifts of the O 1s peaks. The O 1s peaks in Figure S3c,f,h,l can be deconvoluted into two peaks: Si–O at 532.4–532.7 eV and Ti–O at 530.6–531.0 eV. Typically, the O 1s peak of pure silica is centered around 533 eV.[45,60] When titania is added to the network, the binding energy shifts to lower eV as a result of adding a less electronegative species in the network. A clear second peak appears at about 530.5 eV when the concentration of titania exceeds 10 wt % (∼8 mol %) because of the formation of phase-separated Ti–O–Ti bonds. This peak continues to slowly shift to 329 eV as the concentration of titania increases toward a pure titania network. It is therefore not a surprise that the Ti–O peak in the ST20 films (binding energies 530.8 eV (ST20reg) and 530.6 eV (ST20mod)) were lower than those of the ST10 films (binding energies 530.9 eV (ST10reg) and 531.0 eV (ST10mod). In agreement with the NMR data, the sample that should have the most Si–O–Ti bonds (ST10mod) also showed the highest Ti–O binding energy. Moreover, as expected, the ST20 films (with Si–O:Ti–O ratios of 87:13 and 85:15 for ST20reg and ST20mod, respectively) also contained a larger fraction of Ti–O bonds than the ST10 films (with Si–O:Ti–O ratios of 93:07 for both ST10reg and ST10mod). Interestingly, however, the composition of Si derived from the Si–O:Ti–O ratios is larger than those previously derived from the Si 2p:Ti 2p peak areas. This is likely due to the fact that oxygen in mixed Si–O–Ti bonds can appear under the Si–O envelope at low Ti concentrations.[61,62] In addition to the larger ratios of Si, the ratios of O/(Si + Ti) of all samples are greater than 2. These superstoichiometric ratios indicate the presence of extra oxygen in the network, most likely from surface hydroxyl groups in these porous, high-surface-area networks. The –OH peak positions overlap with the Si–O and Ti–O peaks, so we were unable to accurately determine the concentration of hydroxyl groups on the surface. Overall, XPS corroborates many of the conclusions about mixing and elemental composition drawn from NMR and EDS and provides further insight into defect density and surface structure.

The porosity and pore size distribution of the mesoporous silica–titania network were quantified using ellipsometric porosimetry[63] at room temperature with toluene as the adsorbate, and by an interferometry-based technique.[64] Figure 4a shows that the porosity of the films increased from 24 to 60% as more Pluronic F127 was added until the polymer/inorganic mass ratio (m_{poly}/m_{inor}) reached 2.2. Beyond this limit, we observed a decrease in porosity for the ST10reg samples, likely due to increased pore shrinkage during calcination, so 2.2 was set as the limit for all other materials. Figure 4b shows typical adsorption–desorption isotherms for ST20mod samples made with different amounts of polymer. According to the IUPAC classification, all isotherms were of type IV(a) with H2(b) hysteresis loops, signifying that the films were mesoporous with some pore blocking.[65,66] Figure 4c shows that the average pore radii ranged between 2 and 3 nm, and the pore radius distribution broadened as the amount of polymer template increased.
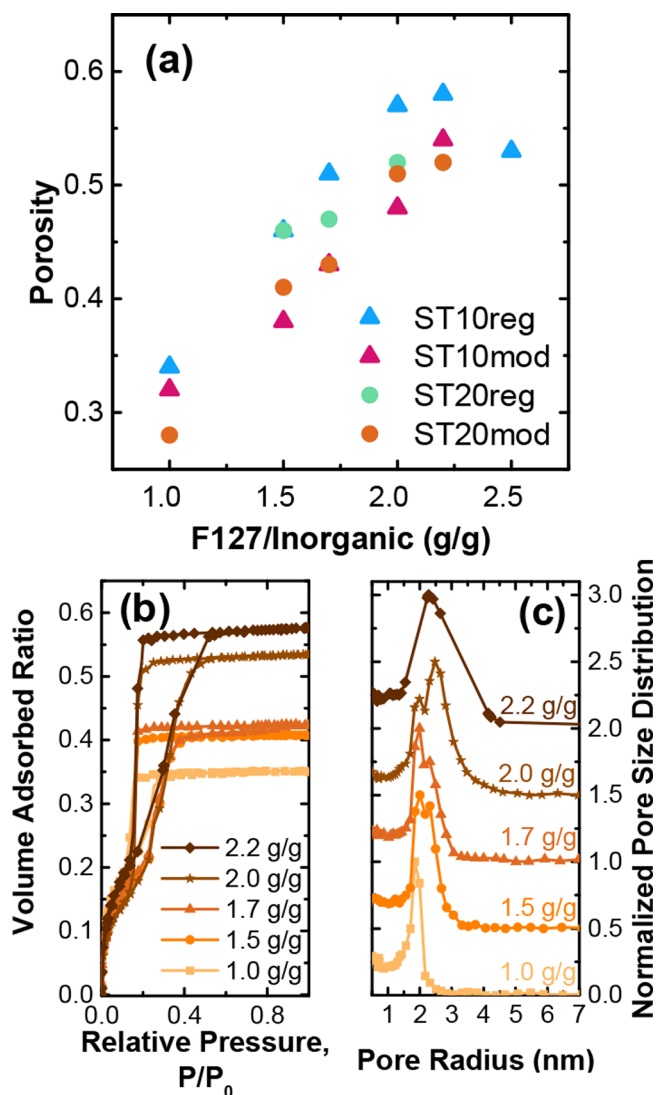

Figure 4. Characterization of the pore structure of the films studied. (a) Porosity as a function of Pluronic F127/(silica + titania) mass ratio for all silica–titania films studied. (b) Toluene adsorption–desorption isotherms and (c) pore size distribution curves for ST20mod samples made from different F127/(silica + titania) mass ratios (given on each graph). Pore size distribution curves are offset by 0.5 units. Overall, total porosity, pores size, and pore heterogeneity all increase as the relative fraction of polymer template increases up to a F127/inorganic mass ratio of 2.2 g/g.

To further examine the effect of polymer addition on the structure of the silica–titania network, two-dimensional grazing incidence X-ray scattering (2D-GISAXS) experiments were performed. Figures 5a–d show 2D-GISAXS patterns of typical ST10 and ST20 films made using both synthetic methods. The full arc in the q_x and q_y directions indicates that all films had ordered porosity, both in the plane of the film and perpendicular to the substrate, in the out-of-plane direction. Figures 5e and 5f plot the reduced 1D graphs that resulted from integrating the intensities of the 2D-GISAXS patterns at 10°–30° and 70°–90° from the origin. These 1D graphs provide information about the pore repeat distance both in- and out-of-plane. For all samples, the out-of-plane peaks are at higher q than the in-plane peaks, indicating that the pores shrink normal to the substrate. The out-of-plane peaks also have lower intensities as a result of the finite film thickness.
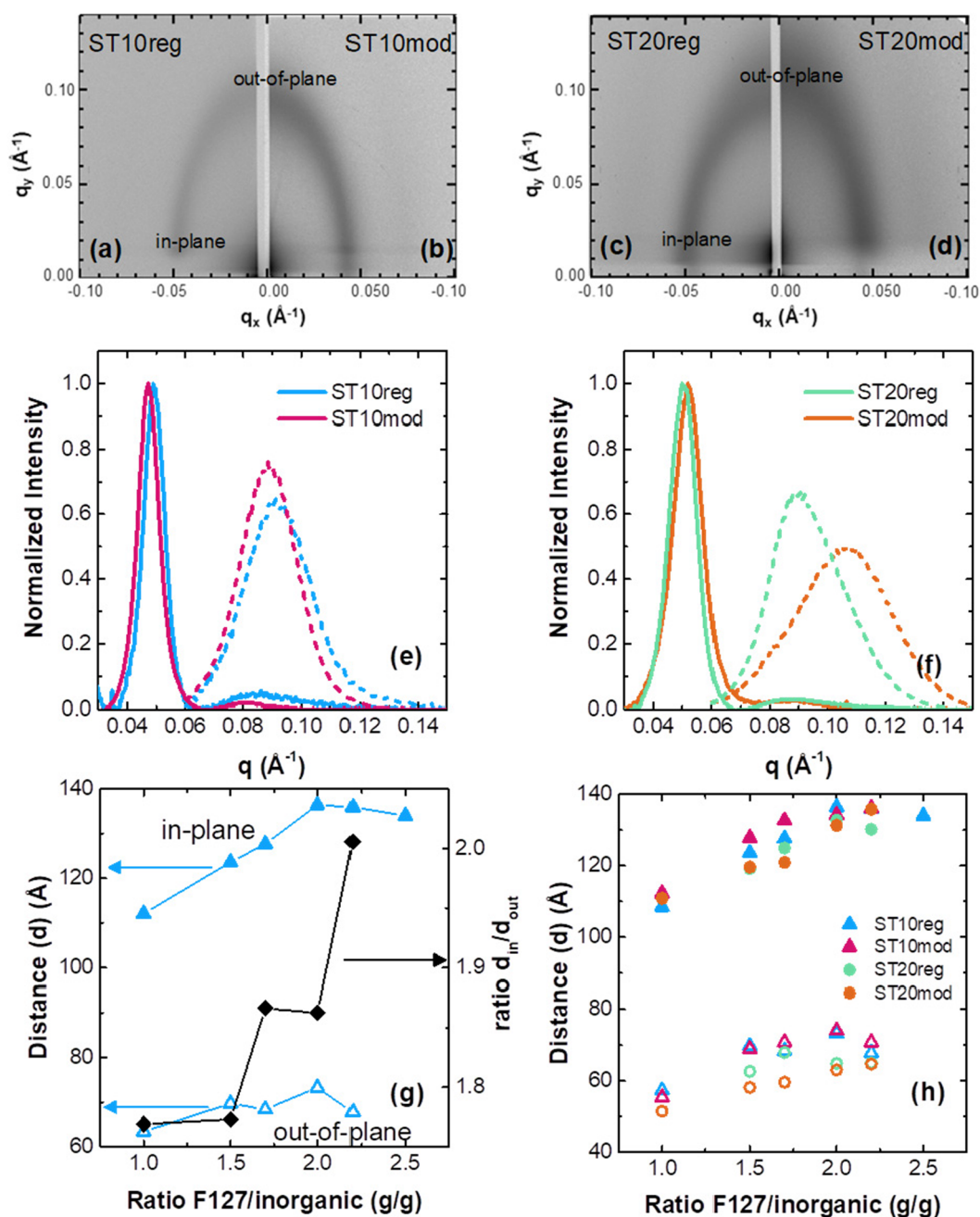
Figure 5. (a–d) Two-dimensional grazing incidence small-angle X-ray scattering (2D-GISAXS) pattern from typical (a) ST10reg, (b) ST10mod, (c) ST20reg, and (d) ST20mod samples. (e, f) The one-dimensional scattering profiles obtained by integrating the intensities of the 2D-GISAXS patterns over the angular range 10°–30° (in-plane) and 70°–90° (out-of-plane) for the ST10 and ST20 samples, respectively. (g) In-plane and out-of-plane pore-repeat distances and the ratio of those two distances as a function of polymer:silica mass ratio for the ST10reg samples. (h) In-plane and out-of-plane distances as a function of polymer:silica mass ratio for all silica–titania samples studied here.

The in-plane data show a weak peak at around 0.09 Å^{-1}, in addition to the main peak at around 0.05 Å^{-1}. These peaks can be indexed to the 100 and 110 planes of a hexagonal lattice (space group $p6mm$) with a ratio of $1:\sqrt{3}$.[43,67–69] Compared to the other silica–titania samples, the out-of-plane peak of the ST20mod occurs at slightly higher q, indicating additional pore shrinkage in the ST20mod samples. Other than this shift, the data for the 10% and 20% titania samples are nearly identical, indicating that these samples are all structurally similar at the nanoscale.

Figure 5g shows the gradual increase in the in- and out-of-plane pore-repeat distances for all m_{poly}/m_{inor} ratios less than 2.0 for the ST10reg series. When $m_{poly}/m_{inor} > 2.0$, the in- and out-of-plane spaces both begin to decrease, presumably because of pore collapse upon heating due to the very thin walls. Additionally, as the amount of polymer added to the composite increased, so did the pore anisotropy, with much smaller pores sizes observed in the out-of-plane direction. This trend continued up to $m_{poly}/m_{inor} = 2.5$, which showed no out-of-plane diffraction, suggesting either total pore collapse or disordering in the out-of-plane direction. This destruction of

the pore order along with the decrease in porosity of the ST10reg sample at m_{poly}/m_{inor} = 2.5 shown in Figure 4a lead us to limit all other syntheses in this work to m_{poly}/m_{inor} ratios less than 2.5. Figure 5h shows similar in- and out-of-plane distances as a function of m_{poly}/m_{inor} for all materials used in this work. Similar trends are observed in all materials.

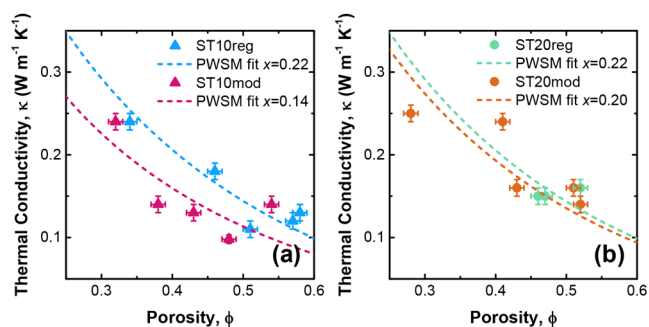**Effect of Compositional Heterogeneity on the Thermal Conductivity.** Figure 6 plots the thermal con-

Figure 6. Effect of chemical homogeneity and fractional porosity on the thermal conductivity of mesoporous mixed silica−titania thin films synthesized with (a) 10 mol % and (b) 20 mol % titania. Here κ refers to κ_{eff}, as defined below.

ductivity as a function of porosity for all mesoporous silica−titania films used in this work. Figure 6a shows that at comparable porosities, the modified samples with their homogeneous titania distribution (ST10mod) have lower thermal conductivities than their less homogeneous counterparts (ST10reg). As established by the ^{29}Si NMR and FTIR spectra of Figures 3a−c, at a titania concentration of 10%, the modified films contain more homogeneously distributed Ti scattering centers than those synthesized using the regular method. In amorphous materials, heat is transported mainly by the propagons and diffusons. The former are similar to phonons in crystalline materials while the latter stem from the diffusion of vibrational modes.[11] The homogeneously distributed titania apparently serve as effective scattering centers for propagons and thus reduce their mean free path. Moreover, the more homogeneous the distribution of heteroatoms, the higher the degree of atomic disorder in the material. As a result, we hypothesize that this homogeneous distribution of heteroatoms results in a higher degree of randomness of vibrational modes, which reduces the thermal coupling of different modes and impedes the diffusion of thermal energy.

On the other hand, Figure 6b shows that the cross-plane thermal conductivities of the ST20reg and ST20mod films were nearly identical at similar porosities. As illustrated in Figures 3d−f, the homogeneities of these samples were very similar, despite differences in their syntheses. This is likely due to fact that the titania concentration exceeds the solubility limit in all ST20 silica−titania composite, resulting in a similarly inhomogeneous distribution of titania scattering centers. This supports the idea that the lower thermal conductivity of the ST10mod film compared with ST10reg is due to higher homogeneity and not due to other effects originating from the differences in the two synthetic methods.

These trends can be quantified by fitting the data in Figures 6a and 6b with the porosity weighted simple medium (PWSM) model (dashed lines in Figure 6) to show the effects of titania concentration and heterogeneity on the thermal conductivity

of the porous network. The PWSM model is often used to qualitatively describe heat conduction in porous material,[70] according to the following equation.

$$\kappa_{eff} = \kappa_{dense}(1 - \phi)(1 - \phi^x)$$

Here, κ_{eff} and κ_{dense} correspond to the thermal conductivity of the porous and analogous fully dense material, ϕ is the porosity, and x is an empirical fitting parameter that can vary from 0 to 1 to indicate the alignment of the heat conducting components of the sample. When $x = 0$, it indicates that the heat conduction components are fully aligned in series while $x = 1$ indicates parallel alignment. By fitting our data to the PWSM model, we determined that the less well mixed ST10reg, ST20reg, and ST20mod samples all have similar PWSM fits with $x = 0.22$, 0.22, and 0.20, respectively. On the other hand, the ST10mod samples, with the more homogeneously distributed titania, produced a PWSM fit of $x = 0.14$, suggesting that the ST10mod films conduct heat in a more serial manner, likely due to increased heat carrier scattering that prevents effective parallel heat conduction. Overall, these results suggest that for the same concentration of atomic defects smaller, more dispersed scattering centers are better at reducing thermal conductivity than larger, less dispersed ones.

Figure 7 compares the thermal conductivity of the present silica−titania composite films with that of mesoporous
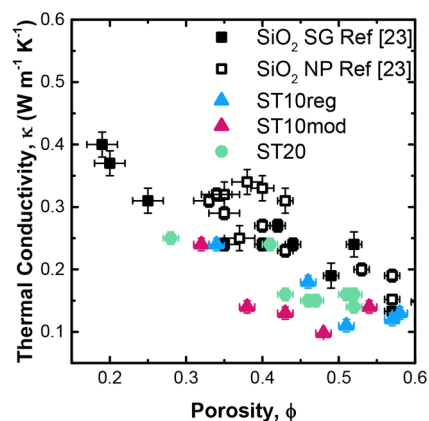

Figure 7. Porosity-dependent thermal conductivity comparing F127 templated mesoporous silica−titania to F127 templated mesoporous silica samples from ref 23 made from continuous sol−gel and discrete nanoparticle-based precursors. The ST20reg and ST20mod samples were combined and all labeled as ST20, since the differences in synthesis did not result in any significant difference in the thermal conductivity.

nanoparticle-based and sol−gel silica films reported from ref 23 that were synthesized using similar methods with F127 block copolymer as the template. The data show that adding either 10 or 20 mol % titania resulted in reduced thermal conductivity compared to the pure silica films, presumably because all Ti incorporation provides additional centers that scattered propagons and diffusons, thus reducing the thermal conductivity of those samples, regardless of the compositional homogeneity. In agreement with this idea, PWSM fits to pure silica samples, published previously, produce a value of $x = 0.31$, which is higher than any of the titania-containing samples.[26] This suggests that all titania incorporation frustrates parallel heat conduction. When we further compare all the samples that show titania clustering, that is, the ST10reg

sample and all ST20 samples, we observe that the ST20 samples had lower thermal conductivities than the ST10reg samples. We hypothesize that this occurred because the ST20 samples have overall more heat carrier scattering sites than the ST10reg samples, thereby lowering the thermal conductivity. However, the more homogeneously distributed ST10mod samples showed the lowest thermal conductivity of all of them, even compared to the ST20 samples that have a higher concentration of Ti. These data suggest that for lowering thermal conductivity, having more dispersed heat carrier scattering centers is overall more effective than adding a larger mole fraction of potential scattering sites.

■ CONCLUSIONS

This study furthers our understanding of heat carrier propagation in amorphous porous materials and introduces new design rules for insulating materials and coatings. From our data, we found that adding titania to the silicate matrix lowers the thermal conductivity of the matrix as a result of introducing additional heat-carrier scattering centers. By comparing both the concentration and the compositional heterogeneity of the scattering sites, we found that the most chemically homogeneous materials with the most distributed scattering sites were more efficient at reducing heat carrier transport than samples with inhomogeneous distributions of scattering centers at either equivalent or higher concentrations. This indicates that the effect of atomic homogeneity is greater than the effect of the total concentration of the heat carrier scattering centers.

Because theories of thermal transport for amorphous materials, particularly when combined with nanoscale porosity, are less developed than those for crystalline materials, this work adds porosity-dependent data on well-characterized materials that can be used for future modeling studies. It is our hope that the thermal transport data on materials with both more and less homogeneously distributed titanium atoms, in particular, will be helpful in understanding the factors that control heat carrier scattering in amorphous materials, where classic phonon transport mechanisms are not applicable.

■ ASSOCIATED CONTENT

Ⓢ Supporting Information

The Supporting Information is available free of charge at https://pubs.acs.org/doi/10.1021/acs.jpcc.0c06697.

> Details of synthesis, structural characterization, and thermal conductivity measurement; tables of synthesis, NMR analysis, and specific heat capacities used in thermal conductivity calculation; additional EDS maps with analysis for Si and Ti content; representative XPS spectra; reduced 2D-GIWAXS patterns (PDF)

■ AUTHOR INFORMATION

Corresponding Author

Sarah H. Tolbert − *Department of Chemistry and Biochemistry, California NanoSystems Institute, and Department of Materials Science and Engineering, University of California, Los Angeles, Los Angeles, California 90095-1569, United States;* ⓞ orcid.org/0000-0001-9969-1582; Phone: (310) 206-4767; Email: tolbert@chem.ucla.edu

Authors

Sophia C. King − *Department of Chemistry and Biochemistry, University of California, Los Angeles, Los Angeles, California 90095-1569, United States*

Man Li − *Department of Mechanical Engineering, University of California, Los Angeles, Los Angeles, California 90095-1597, United States*

Tiphaine Galy − *Department of Mechanical Engineering, University of California, Los Angeles, Los Angeles, California 90095-1597, United States*

Yan Yan − *Department of Chemistry and Biochemistry, University of California, Los Angeles, Los Angeles, California 90095-1569, United States*

Joon Sang Kang − *Department of Mechanical Engineering, University of California, Los Angeles, Los Angeles, California 90095-1597, United States*

Victoria M. Basile − *Department of Chemistry and Biochemistry, University of California, Los Angeles, Los Angeles, California 90095-1569, United States*

Yolanda L. Li − *Department of Chemistry and Biochemistry, University of California, Los Angeles, Los Angeles, California 90095-1569, United States*

Michal Marszewski − *Department of Mechanical Engineering, University of California, Los Angeles, Los Angeles, California 90095-1597, United States;* ⓞ orcid.org/0000-0002-4157-3046

Laurent Pilon − *Department of Mechanical Engineering, Institute of the Environment and Sustainability, and California NanoSystems Institute, University of California, Los Angeles, Los Angeles, California 90095-1597, United States;* ⓞ orcid.org/0000-0001-9459-8207

Yongjie Hu − *Department of Mechanical Engineering, University of California, Los Angeles, Los Angeles, California 90095-1597, United States*

Complete contact information is available at:
https://pubs.acs.org/10.1021/acs.jpcc.0c06697

Notes

The authors declare no competing financial interest.

■ ACKNOWLEDGMENTS

■ REFERENCES

(1) Randall, J. P.; Meador, M. A. B.; Jana, S. C. Tailoring Mechanical Properties of Aerogels for Aerospace Applications. *ACS Appl. Mater. Interfaces* **2011**, *3*, 613−626.

(2) Marszewski, M.; King, S. C.; Yan, Y.; Galy, T.; Li, M.; Dashti, A.; Butts, D. M.; Kang, J. S.; McNeil, P. E.; Lan, E.; et al. Thick Transparent Nanoparticle-Based Mesoporous Silica Monolithic Slabs for Thermally Insulating Window Materials. *ACS Appl. Nano Mater.* **2019**, *2*, 4547−4555.

(3) Kwon, Y. G.; Choi, S. E. Y.; Kang, E. S.; Baek, S. S. U. Ambient-Dried Silica Aerogel Doped with TiO$_2$ Powder for Thermal Insulation. *J. Mater. Sci.* **2000**, *35*, 6075−6079.

(4) Marino, K. A.; Hinnemann, B.; Carter, E. A. Atomic-Scale Insight and Design Principles for Turbine Engine Thermal Barrier Coatings from Theory. *Proc. Natl. Acad. Sci. U. S. A.* **2011**, *108*, 5480−5487.

(5) Klemens, P. G.; Gell, M. Thermal Conductivity of Thermal Barrier Coatings. *Mater. Sci. Eng., A* **1998**, *245*, 143−149.

(6) Padture, N. P.; Gell, M.; Jordan, E. H. Thermal Barrier Coatings for Gas-Turbine Engine Applications. *Science* **2002**, *296*, 280−284.

(7) Jarvis, E. A.; Carter, E. A. The Role of Reactive Elements in Thermal Barrier Coatings. *Comput. Sci. Eng.* **2002**, *4*, 33−41.

(8) Tritt, T. M. *Thermal Conductivity Theory, Properties and Applications*; Kluwer Academic/Plenum Publishers: New York, 2004.

(9) Cahill, D. G.; Ford, W. K.; Goodson, K. E.; Mahan, G. D.; Majumdar, A.; Maris, H. J.; Merlin, R.; Phillpot, S. R. Nanoscale Thermal Transport. *J. Appl. Phys.* **2003**, *93*, 793−818.

(10) Cahill, D. G.; Braun, P. V.; Chen, G.; Clarke, D. R.; Fan, S.; Goodson, K. E.; King, W. P.; Mahan, G. D.; Majumdar, A.; Maris, H. J.; et al. Nanoscale Thermal Transport. II. 2003−2012. *Appl. Phys. Rev.* **2014**, *1*, 011305.

(11) Allen, P. B.; Feldman, J. L.; Fabian, J.; Wooten, F. Diffusons, Locons and Propagons: Character of Atomic Vibrations in Amorphous Si. *Philos. Mag. B* **1999**, *79*, 1715−1731.

(12) Wingert, M. C.; Zheng, J.; Kwon, S.; Chen, R. Thermal Transport in Amorphous Materials: A Review. *Semicond. Sci. Technol.* **2016**, *31*, 113003.

(13) Zhou, W.; Cheng, Y.; Chen, K.; Xie, G.; Wang, T.; Zhang, G. Thermal Conductivity of Amorphous Materials. *Adv. Funct. Mater.* **2020**, *30*, 1903829.

(14) Zhang, H.; Hua, C.; Ding, D.; Minnich, A. J. Length Dependent Thermal Conductivity Measurements Yield Phonon Mean Free Path Spectra in Nanostructures. *Sci. Rep.* **2015**, *5*, 9121.

(15) Hu, Y.; Zeng, L.; Minnich, A. J.; Dresselhaus, M. S.; Chen, G. Spectral Mapping of Thermal Conductivity through Nanoscale Ballistic Transport. *Nat. Nanotechnol.* **2015**, *10*, 701−706.

(16) Tsui, B.-Y.; Yang, C.-C.; Fang, K.-L. Anisotropic Thermal Conductivity of Nanoporous Silica Film. *IEEE Trans. Electron Devices* **2004**, *51*, 20−27.

(17) Hrubesh, L. W.; Pekala, R. W. Thermal Properties of Organic and Inorganic Aerogels. *J. Mater. Res.* **1994**, *9*, 731−738.

(18) Gross, J.; Reichenauer, G.; Fricke, J. Mechanical Properties of SiO$_2$ Aerogels. *J. Phys. D: Appl. Phys.* **1988**, *21*, 1447−1451.

(19) Shimizu, T.; Kanamori, K.; Maeno, A.; Kaji, H.; Doherty, C. M.; Falcaro, P.; Nakanishi, K. Transparent, Highly Insulating Polyethyl- and Polyvinylsilsesquioxane Aerogels: Mechanical Improvements by Vulcanization for Ambient Pressure Drying. *Chem. Mater.* **2016**, *28*, 6860−6868.

(20) Kistler, S. S. Coherent Expanded Aerogels and Jellies. *Nature* **1931**, *127*, 741−741.

(21) Rubin, M.; Lampert, C. M. Transparent Silica Aerogels for Window Insulation. *Sol. Energy Mater.* **1983**, *7*, 393−400.

(22) Gunay, A. A.; Kim, H.; Nagarajan, N.; Lopez, M.; Kantharaj, R.; Alsaati, A.; Marconnet, A.; Lenert, A.; Miljkovic, N. Optically Transparent Thermally Insulating Silica Aerogels for Solar Thermal Insulation. *ACS Appl. Mater. Interfaces* **2018**, *10*, 12603−12611.

(23) Yan, Y.; King, S. C.; Li, M.; Galy, T.; Marszewski, M.; Kang, J. S.; Pilon, L.; Hu, Y.; Tolbert, S. H. Exploring the Effect of Porous Structure on Thermal Conductivity in Templated Mesoporous Silica Films. *J. Phys. Chem. C* **2019**, *123*, 21721−21730.

(24) Fang, J.; Reitz, C.; Brezesinski, T.; Nemanick, E. J.; Kang, C. B.; Tolbert, S. H.; Pilon, L. Thermal Conductivity of Highly-Ordered Mesoporous Titania Thin Films from 30 to 320 K. *J. Phys. Chem. C* **2011**, *115*, 14606−14614.

(25) Coquil, T.; Richman, E. K.; Hutchinson, N. J.; Tolbert, S. H.; Pilon, L. Thermal Conductivity of Cubic and Hexagonal Mesoporous Silica Thin Films. *J. Appl. Phys.* **2009**, *106*, 034910.

(26) Yan, Y.; Li, M.; King, S.; Galy, T.; Marszewski, M.; Kang, J. S.; Pilon, L.; Hu, Y.; Tolbert, S. H. Controlling Thermal Conductivity in Mesoporous Silica Films Using Pore Size and Nanoscale Architecture. *J. Phys. Chem. Lett.* **2020**, *11*, 3731−3737.

(27) Lu, X.; Caps, R.; Fricke, J.; Alviso, C. T.; Pekala, R. W. Correlation between Structure and Thermal Conductivity of Organic Aerogels. *J. Non-Cryst. Solids* **1995**, *188*, 226−234.

(28) Emmerling, A.; Fricke, J.; Hubland, A. Scaling Properties and Structure of Aerogels. *J. Sol-Gel Sci. Technol.* **1997**, *8*, 781−788.

(29) Fricke, J.; Lu, X.; Wang, P.; Büttner, D.; Heinemann, U. Optimization of Monolithic Silica Aerogel Insulants. *Int. J. Heat Mass Transfer* **1992**, *35*, 2305−2309.

(30) Callaway, J.; von Baeyer, H. C. Effect of Point Imperfection on Lattice Thermal Conductivity. *Phys. Rev.* **1960**, *120*, 1149−1154.

(31) Callaway, J. Model for Lattice Thermal Conductivity at Low Temperatures. *Phys. Rev.* **1959**, *113*, 1046−1051.

(32) Klemens, P. G. Thermal Resistance Due to Point Defects at High Temperatures. *Phys. Rev.* **1960**, *119*, 507−509.

(33) Klemens, P. G. The Scattering of Low-Frequency Lattice Waves by Static Imperfections. *Proc. Phys. Soc., London, Sect. A* **1955**, *68*, 1113−1128.

(34) Seyf, H. R.; Henry, A. A Method for Distinguishing between Propagons, Diffusions, and Locons. *J. Appl. Phys.* **2016**, *120*, No. 025101.

(35) Choy, C. L.; Tong, K. W.; Wong, H. K.; Leung, W. P. Thermal Conductivity of Amorphous Alloys above Room Temperature. *J. Appl. Phys.* **1991**, *70*, 4919−4925.

(36) Choy, C. L.; Leung, W. P.; Ng, Y. K. Thermal Conductivity of Metallic Glasses. *J. Appl. Phys.* **1989**, *66*, 5335−5339.

(37) Varshneya, A. K.; Mauro, J. C. *Fundamentals of Inorganic Glasses*, 3rd ed.; Elsevier: 2019.

(38) Yoldas, B. E. Introduction and Effect of Structural Variations in Inorganic Polymers and Glass Networks. *J. Non-Cryst. Solids* **1982**, *51*, 105−121.

(39) Woo, H.; Char, K. Transparent Organosilicate Hybrid Films with Thermally Insulating and UV-Blocking Properties Based on Silica/Titania Hybrid Hollow Colloidal Shells. *Macromol. Res.* **2013**, *21*, 1004−1010.

(40) Que, W.; Sun, Z.; Zhou, Y.; Lam, Y. L.; Chan, Y. C.; Kam, C. H. Optical and Mechanical Properties of TiO$_2$/SiO$_2$/Organically Modified Silane Composite Films Prepared by Sol-Gel Processing. *Thin Solid Films* **2000**, *359*, 177−183.

(41) Emili, M.; Incoccia, L.; Mobilio, S.; Fagherazzi, G.; Guglielmi, M. Structural Investigations of TiO$_2$-SiO$_2$ Glassy and Glass-Ceramic Materials Prepared by the Sol-Gel Method. *J. Non-Cryst. Solids* **1985**, *74*, 129−146.

(42) Yoldas, B. E. Formation of Titania-Silica Glasses by Low Temperature Chemical Polymerization. *J. Non-Cryst. Solids* **1980**, *38−39*, 81−86.

(43) Dong, W.; Sun, Y.; Lee, C. W.; Hua, W.; Lu, X.; Shi, Y.; Zhang, S.; Chen, J.; Zhao, D. Controllable and Repeatable Synthesis of Thermally Stable Anatase Nanocrystal-Silica Composites with Highly Ordered Hexagonal Mesostructures. *J. Am. Chem. Soc.* **2007**, *129*, 13894−13904.

(44) Jung, H.; Kim, Y. H.; Kim, J.; Yoon, T. S.; Kang, C. J.; Yoon, S.; Lee, H. H. Analog Memristive Characteristics of Mesoporous Silica-Titania Nanocomposite Device Concurrent with Selection Diode Property. *ACS Appl. Mater. Interfaces* **2019**, *11*, 36807−36816.

(45) Stakheev, A. Y.; Shpiro, E. S.; Apijok, J. XPS and XAES Study of TiO$_2$-SiO$_2$ Mixed Oxide System. *J. Phys. Chem.* **1993**, *97*, 5668−5672.

(46) Delattre, L.; Babonneau, F. ^{17}O Solution NMR Characterization of the Preparation of Sol−Gel Derived SiO$_2$/TiO$_2$ and SiO$_2$/ZrO$_2$ Glasses. *Chem. Mater.* **1997**, *9*, 2385−2394.

(47) Davis, R. J.; Liu, Z. Titania-Silica: A Model Binary Oxide Catalyst System. *Chem. Mater.* **1997**, *9*, 2311−2324.

(48) Liu, Z.; Davis, R. J. Investigation of the Structure of Microporous Ti-Si Mixed Oxides by X-Ray, UV Reflectance, FT-Raman, and FT-IR Spectroscopies. *J. Phys. Chem.* **1994**, *98*, 1253−1261.

(49) Dirken, P. J.; Smith, M. F.; Whitfield, H. J. ^{17}O and ^{29}Si Solid State NMR Study of Atomic Scale Structure in Sol-Gel-Prepared TiO_2-SiO_2 materials. *J. Phys. Chem.* **1995**, *99*, 395−401.

(50) Pickup, D. M.; Mountjoy, G.; Wallidge, G. W.; Anderson, R.; Cole, J. M.; Newport, R. J.; Smith, M. E. A Structural Study of $(TiO_2)_x(SiO_2)_{1−x}$ (x = 0.18, 0.30 and 0.41) Xerogels Prepared Using Acetylacetone. *J. Mater. Chem.* **1999**, *9*, 1299−1305.

(51) Chen, H.; Huang, S.; Perng, T. Preparation and Characterization of Molecularly Homogeneous Silica − Titania Film by Sol − Gel Process with Different Synthetic Strategies. *ACS Appl. Mater. Interfaces* **2012**, *4*, 5188−5195.

(52) Yang, L.-L.; Lai, Y.-S.; Chen, J. S.; Tsai, P. H.; Chen, C. L.; Chang, C. J. Compositional Tailored Sol-Gel SiO_2 − TiO_2 Thin Films: Crystallization, Chemical Bonding Configuration, and Optical Properties. *J. Mater. Res.* **2005**, *20*, 3141−3149.

(53) Dunphy, D. R.; Sheth, P. H.; Garcia, F. L.; Brinker, C. J. Enlarged Pore Size in Mesoporous Silica Films Templated by Pluronic F127: Use of Poloxamer Mixtures and Increased Template/SiO_2 Ratios in Materials Synthesized by Evaporation-Induced Self-Assembly. *Chem. Mater.* **2015**, *27*, 75−84.

(54) Busato, S.; Perevedentsev, A. A Simple Imaging-Based Technique for Quantifying Haze and Transmittance of Materials. *Polym. Eng. Sci.* **2018**, *58*, 345−352.

(55) Calleja, G.; Serrano, D. P.; Sanz, R.; Pizarro, P. Mesostructured SiO_2 -Doped TiO_2 with Enhanced Thermal Stability Prepared by a Soft-Templating Sol − Gel Route. *Microporous Mesoporous Mater.* **2008**, *111*, 429−440.

(56) Chao, S.; Wang, W.-H.; Hsu, M.-Y.; Wang, L.-C. Characteristics of Ion-Beam-Sputtered High-Refractive-Index TiO_2-SiO_2 Mixed Films. *J. Opt. Soc. Am. A* **1999**, *16*, 1477.

(57) Chen, J.-S.; Chao, S.; Kao, J.-S.; Niu, H.; Chen, C.-H. Mixed Films of TiO_2−SiO_2 Deposited by Double Electron-Beam Coevaporation. *Appl. Opt.* **1996**, *35*, 90.

(58) Chao, S.; Chang, C.-K.; Chen, J.-S. TiO_2−SiO_2 Mixed Films Prepared by the Fast Alternating Sputter Method. *Appl. Opt.* **1991**, *30*, 3233.

(59) Xie, C.; Xu, Z.; Yang, Q.; Xue, B.; Du, Y.; Zhang, J. Enhanced Photocatalytic Activity of Titania-Silica Mixed Oxide Prepared via Basic Hydrolyzation. *Mater. Sci. Eng., B* **2004**, *112*, 34−41.

(60) Netterfield, R. P.; Martin, P. J.; Pacey, C. G.; Sainty, W. G.; McKenzie, D. R.; Auchterlonie, G. Ion-assisted Deposition of Mixed TiO_2 -SiO_2 Films. *J. Appl. Phys.* **1989**, *66*, 1805−1809.

(61) Paparazzo, E.; Fanfoni, M.; Severini, E.; Priori, S. Evidence of Si−OH Species at the Surface of Aged Silica. *J. Vac. Sci. Technol., A* **1992**, *10*, 2892−2896.

(62) Paparazzo, E. On the XPS Analysis of Si-OH Groups at the Surface of Silica. *Surf. Interface Anal.* **1996**, *24*, 729−730.

(63) Baklanov, M. R.; Mogilnikov, K. P.; Polovinkin, V. G.; Dultsev, F. N. Determination of Pore Size Distribution in Thin Films by Ellipsometric Porosimetry. *J. Vac. Sci. Technol., B: Microelectron. Process. Phenom.* **2000**, *18*, 1385−1391.

(64) Galy, T.; Marszewski, M.; King, S.; Yan, Y.; Tolbert, S. H.; Pilon, L. Comparing Methods for Measuring Thickness, Refractive Index, and Porosity of Mesoporous Thin Films. *Microporous Mesoporous Mater.* **2020**, *291*, 109677.

(65) Thommes, M.; Kaneko, K.; Neimark, A. V.; Olivier, J. P.; Rodriguez-Reinoso, F.; Rouquerol, J.; Sing, K. S. W. Physisorption of Gases, with Special Reference to the Evaluation of Surface Area and Pore Size Distribution (IUPAC Technical Report). *Pure Appl. Chem.* **2015**, *87*, 1051−1069.

(66) Sing, K. S. W.; Everett, D. H.; Haul, R. A. W.; Moscou, L.; Pierotti, R. A.; Rouquerol, J.; Siemieniewska, T. Reporting Physisorption Data for Gas/Solid Systems with Special Reference to the Determination of Surface Area and Porosity. *Pure Appl. Chem.* **1985**, *57*, 603−619.

(67) Yang, P.; Zhao, D.; Margolese, D. I.; Chmelka, B. F.; Stucky, G. D. Block Copolymer Templating Syntheses of Mesoporous Metal Oxides with Large Ordering Lengths and Semicrystalline Framework. *Chem. Mater.* **1999**, *11*, 2813−2826.

(68) Tian, B.; Liu, X.; Tu, B.; Yu, C.; Fan, J.; Wang, L.; Xie, S.; Stucky, G. D.; Zhao, D. Self-Adjusted Synthesis of Ordered Stable Mesoporous Minerals by Acid−Base Pairs. *Nat. Mater.* **2003**, *2*, 159−163.

(69) Li, D.; Zhou, H.; Honma, I. Design and Synthesis of Self-Ordered Mesoporous Nanocomposite through Controlled in-Situ Crystallization. *Nat. Mater.* **2004**, *3*, 65−72.

(70) Pietrak, K.; Wisniewski, T. S. A Review of Models for Effective Thermal Conductivity of Composite Materials. *J. Power Technol.* **2015**, *95*, 14−24.